

Near-field multiple super-resolution imaging from Mikaelian lens to generalized Maxwell's fish-eye lens

Yangyang Zhou(周杨阳), and Huanyang Chen(陈焕阳)†

Citation: Chin. Phys. B, 2022, 31 (**10**): 104205. DOI: 10.1088/1674-1056/ac5d34
Journal homepage: http://cpb.iphy.ac.cn; http://iopscience.iop.org/cpb

What follows is a list of articles you may be interested in

Deep-learning-based cryptanalysis of two types of nonlinear optical cryptosystems

Xiao-Gang Wang(汪小刚) and Hao-Yu Wei(魏浩宇)
Chin. Phys. B, 2022, 31 (**9**): 094202. DOI: 10.1088/1674-1056/ac6331

Imaging a periodic moving/state-changed object with Hadamard-based computational ghost imaging

Hui Guo(郭辉), Le Wang(王乐), and Sheng-Mei Zhao(赵生妹)
Chin. Phys. B, 2022, 31 (**8**): 084201. DOI: 10.1088/1674-1056/ac6498

An apodized cubic phase mask used in a wavefront coding system to extend the depth of field

Lina Zhu(朱丽娜), Fei Li(李飞), Zeyu Huang(黄泽宇), and Tingyu Zhao(赵廷玉)
Chin. Phys. B, 2022, 31 (**5**): 054217. DOI: 10.1088/1674-1056/ac5979

Color-image encryption scheme based on channel fusion and spherical diffraction

Jun Wang(王君), Yuan-Xi Zhang(张沅熙), Fan Wang(王凡), Ren-Jie Ni(倪仁杰), and Yu-Heng Hu(胡玉衡)
Chin. Phys. B, 2022, 31 (**3**): 034205. DOI: 10.1088/1674-1056/ac1b87

Possibility to break through limitation of measurement range in dual-wavelength digital holography

Tuo Li(李拓), Wen-Xiu Lei(雷文秀), Xin-Kai Sun(孙鑫凯), Jun Dong(董军), Ye Tao(陶冶), and Yi-Shi Shi(史祎诗)
Chin. Phys. B, 2021, 30 (**9**): 094201. DOI: 10.1088/1674-1056/abf348

SPECIAL TOPIC — Optical field manipulation

Near-field multiple super-resolution imaging from Mikaelian lens to generalized Maxwell's fish-eye lens

Yangyang Zhou(周杨阳) and Huanyang Chen(陈焕阳)†

Institute of Electromagnetics and Acoustics and Department of Physics, College of Physical Science and Technology, Xiamen University, Xiamen 361005, *China*

(Received 3 February 2022; revised manuscript received 25 February 2022; accepted manuscript online 14 March 2022)

Super-resolution imaging is vital for optical applications, such as high capacity information transmission, real-time bio-molecular imaging, and nanolithography. In recent years, technologies and methods of super-resolution imaging have attracted much attention. Different kinds of novel lenses, from the superlens to the super-oscillatory lens, have been designed and fabricated to break through the diffraction limit. However, the effect of the super-resolution imaging in these lenses is not satisfactory due to intrinsic loss, aberration, large sidebands, and so on. Moreover, these lenses also cannot realize multiple super-resolution imaging. In this research, we introduce the solid immersion mechanism to Mikaelian lens (ML) for multiple super-resolution imaging. The effect is robust and valid for broadband frequencies. Based on conformal transformation optics as a bridge linking the solid immersion ML and generalized Maxwell's fish-eye lens (GMFEL), we also discovered the effect of multiple super-resolution imaging in the solid immersion GMFEL.

Keywords: multiple super-resolution imaging, Mikaelian lens, generalized Maxwell's fish-eye lens, conformal transformation optics

PACS: 42.30.–d, 78.67.Pt **DOI:** 10.1088/1674-1056/ac5d34

1. Introduction

The resolution of the conventional lens is inherently constrained by the diffraction limit, wherein the spatial information of features smaller than one-half of the wavelength exponentially decays and cannot be transferred to the far field. Although near-field scanning optical microscope has achieved super-resolution by collecting the evanescent field in close proximity to the object,[1] this serial technique suffers from the slow scanning speed and non-negligible near-field perturbation preventing its application in real-time imaging. A perfect lens,[2] relying on negative index materials[3,4] to restore evanescent wave at the imaging point, as a first step towards real-time imaging was proposed. Following the concept of the perfect lens, a series of superlenses[5–11] were fabricated to project the sub-diffraction-limited imaging at the near field of the superlens. Later, a hyperlens[12] was designed to far-field super-resolution imaging by metamaterials with hyperbolic dispersion supporting the propagating waves with very large spatial wave vector. Utilizing alternating metal–dielectric structure in a curved geometry and other metamaterial structures, optical hyperlenses were fabricated[13–15] to project the sub-diffraction-limited magnified imaging at the far-field. However, for these designs both the superlens and hyperlens, insurmountable manufacturing challenges and intrinsic losses from the lens are big obstacles to the applications.

Recently, a series of super-oscillation lenses (short as SOLs)[16–18] have been designed and fabricated to achieve super-resolution focusing without evanescent waves based on optical super-oscillation theory.[19,20] From theoretical analysis, we can conclude that the resolution of SOL goes to infinity. However, with the resolution increasing, a large sidebands will emerge at the focus spots, which will severely constrain the focusing efficiency. Moreover, the working bandwidth of SOL is limited to single frequency or some discrete frequency points, which is another obstacle. As another super-resolution lens, solid immersion lens (SIL)[21,22] has been studied extensively through the application of high refractive index (RI) solid material and specific geometric optical design.[23–25] The SIL improves the imaging resolution utilizing high RI materials to transfer electromagnetic waves with high spatial frequency to the imaging point. So far, many types of SILs have been developed from conventional structures to novel metamaterials structures.[26–28] However, chromatic aberration constrains the applications scope of SIL.

Gradient refractive index (GRI) lens has been developed rapidly for its excellent capability to control the propagation of electromagnetic waves[29–33] and enable focusing or imaging.[34–41] Among these GRI lenses, the Mikaelian lens (ML) as a self-focusing cylindrical medium was derived firstly by Mikaelian in 1951[42] and has drawn much attention, due to its property of self-imaging in geometrical optics.[43,44] Many applications based on the Mikaelian lens were designed and fabricated from microwave frequency to optical frequency.[43,45,46]

†Corresponding author. E-mail: kenyon@xmu.edu.cn

© 2022 Chinese Physical Society and IOP Publishing Ltd

In this work, we proposed a solid immersion Mikaelian lens (SIML) and proved that the SIML can achieve near-field multiple super-resolution real-time imaging. We found that SIML provides achromatic aberration imaging. Using conformal transformation,[47,48] the SIML was transformed into a modified solid immersion generalized Maxwell's fish-eye lens (SIGMFEL), which can also realize multiple super-resolution imaging. Although a drain-assisted GMFEL[49] with extreme RI profile also can achieve subwavelength imaging, the drain located at the imaging position hinders the information collection of the target object, and at same time the information of the imaging includes both from the object and from the drain which the imaging is no longer an intrinsic property of GMFEL. Different from the drain-assisted GMFEL, this modified SIGMFEL only alters the RI profile, maintains the intrinsic property of GMFEL and circumvents complex drain. The modified SIGMFEL is easier to realize due to its RI profile with a feasible range compared with drain-assisted GMFEL and conventional generalized Maxwell's fish-eye lens (GMFEL).[50,51] We will start from a semi-infinite SIML and analyze the super-resolution imaging performance of the SIML. Considering practical applications, a truncated SIML with finite size and RI distribution of feasible range was proposed and can maintain the super-resolution imaging performance to the level of semi-infinite SIML. Later on, utilizing conformal transformation, a modified SIGMFEL was designed for multiple super-resolution imaging based on the truncated SIML. The designed truncated SIML and modified SIGMFEL eliminates the extreme RI. Numerical simulation is employed to prove the validity of super-resolution imaging by commercial software COMSOL Multiphysics.

2. Results and discussion

Generally, the Mikaelian lens (ML)[42] is a cylindrical lens, whose RI profile satisfies $n_0\,\mathrm{sech}(\beta r)$ and decreases gradually from the center to the edge in the radial direction, where r is radial distance and n_0 is the maximum RI along the symmetric axis, β is the gradient coefficient which determines the focusing period of the lens $L = 2\pi/\beta$. For a two-dimensional case, the RI can be written as (assuming the symmetric axis is along the y axis)

$$n = n_0\,\mathrm{sech}(\beta x), \tag{1}$$

where n conventionally set as 1 and the RI on the symmetric axis matching RI of the air background. In this case, figure 1(a) shows one-half of conventional ML (with $n = 1$, $\beta = 1$) located in the region of $(0 \le x < \infty, 0 \le y \le 5L/2)$ in the air, and no reflection and evanescent wave emerge at lens/air interface. Light rays propagate along a sine-like path focusing and the RI profile of ML is shown in Fig. 1(a). Different from Fig. 1(a), figure 1(b) introduces impedance mismatching at the lens/air interface by changing $n = 3$ and the evanescent wave is ignited at the interface. Due to total internal reflection (TIR) at the edge of the lens, light rays realize multiple focusing points along the edge of the lens as shown in Fig. 1(b). By full-wave simulation, we analyze field intensity profile of the SIML and its performance of imaging at the wavelength of 10 (a.u.). Figures 1(c) and (d) show the field intensity profile of the conventional ML and SIML and the corresponding full width at half maximum (FWHM) of which a point source (line current) (located at $x = 0$, $y = L/2$) excites a transverse electric (TE) cylindrical wave in the lens, respectively. In figures, the solid red curves represent normalized electric field intensity along the y-axis direction at air imaging plane and the related FWHMs are marked as well. Clearly, the corresponding FWHM decreases from 0.98λ to 0.39λ with $n = 1$ increasing to 3. It reveals that the resolution of the SIML is below the diffraction limit 0.5λ and keeps the sub-diffraction resolution along the edge of the lens in multiple focusing points. Predictably, the ML can achieve super-resolution imaging.

To further verify the super-resolution imaging of SIML, a pair of identical sources with a spacing of $(1/3)\lambda$ are located at the interface of the lens to excite a TE cylindrical wave at wavelength of 10 as shown in Fig. 1(f). It shows that the SIML resolves the two-point sources and realizes super-imaging successfully. In the figure, the red solid curve illustrates the normalized field intensity along the y-axis direction from L to $L/5$ and $x = -1$ at the air. As comparison, the conventional ML interact with a pair of identical sources with a spacing of $(1/3)\lambda$ as shown in Fig. 1(c). From the figure, the conventional ML fails to distinguish the two-point sources, because the electromagnetic waves with larger wave number than one of vacuum exponentially decay and cannot propagate into far-field imaging point.[40] By contrast, the semi-infinite SIML successfully realizes super-resolution imaging and the solid immersion mechanism is valid for improving the resolution of the lens. However, this semi-infinite SIML is difficult for fabrication and application. The RI profile of the lens along the x-axis direction gradually decreases to 0. To circumvent the problem, we truncate the semi-infinite SIML into finite width to adjust RI ranging from 3 to 1 along the x-axis direction, as shown in Figs. 1(g) and 1(h). The truncated SIML is located in the region of $(0 \le x \le \mathrm{arccosh}(3), 0 \le y \le 5L/2)$. The truncated SIML performance of super-resolution imaging is shown in Figs. 1(h) and 1(j). Obviously, the functionality of the truncated SIML is identical with that of the semi-infinite SIML. As a comparison, the imaging of the truncated conventional ML is plot in Figs. 1(g) and 1(i). The size of the truncated conventional ML is the same as that of the truncated SIML and the black solid line represents the boundary of the lens. In the figures, the truncated conventional ML fails to realize super-resolution imaging.

Using an exponential conformal mapping[47,51] $w = \exp(-z(x,y))$, a SIGMFEL was designed based on the above semi-finite SIML with the RI profile $n = n_0 \operatorname{sech}(\beta x)$ where $n = 3$. We can obtain the RI profile of the SIGMFEL in u–v space according to the following formula:

$$n_{\mathrm{w}} = n_z \left| \frac{\mathrm{d}z}{\mathrm{d}w} \right|. \tag{2}$$

By calculation, the RI profile of the designed SIGMFLE is

$$n = \frac{2n_0}{(r/R)^{1+\beta} + (r/R)^{1-\beta}},$$

where r is the distance from the center of the lens and n represents ambient RI, and R denotes the radius of SIGMFEL. Therefore, we derive the RI profile of the SIGMFEL. According to transformation optics, we can deduce that the SIGMFEL also achieves super-resolution imaging. To verify the super-resolution imaging performance of the SIGMFEL, we choose three different semi-finite SIMLs with $\beta = 0.8$, 1, and 1.7 and transformed the three SIMLs into three circular SIGMFELs respectively, as shown in Figs. 2(a)–2(c). The size of these SIGMFELs are same and the corresponding radius is 60. Light rays and the related RI profiles are shown in the figures. For $\beta = 0.8$ and 1.7, all the rays emitting from the point source are converging at the two different points as present in Figs. 1(a) and 1(c), respectively. For $\beta = 1$, the GMFEL becomes well-known MFEL[40] and can focus all light rays from a point source into the opposite point and the RI decrease from 6 (at the center) to 3 (at the edge), as shown Fig. 2(b). A part of light rays are reflected at the edges of lenses due to impendence mismatching at the lens/air interfaces. The ambient RI of the three lenses is $n = 3$. Next, we will stimulatingly calculate the super-resolution imaging of three different SIGMFEL at the wavelength of 10. A point source (line current) is located at $x = -60$, $y = 0$ (the center of the SIGMFEL is located at the origin) to excite a TE cylindrical wave. Figures 1(d)–1(f) show the electric field intensity patterns and the corresponding FWHMs of the three different GMFEL with $\beta = 0.8$, 1, and 1.7 respectively. In the figures, the red curves display the electric field intensity at the imaging plane and the related FWHM of the imaging point in air. Notably, the corresponding FWHM is less than 0.2λ which is far below the diffraction limit 0.5λ at the wavelength of 10 for the three lenses. It demonstrates that the three GMFELs achieve super-imaging successfully.

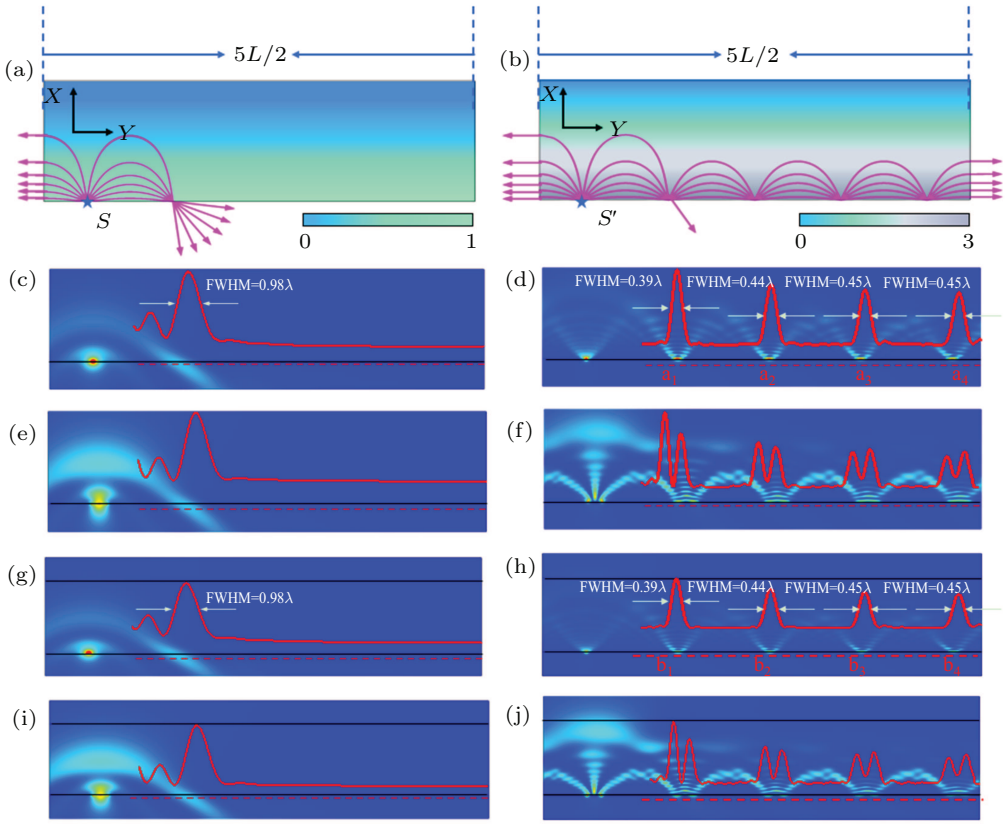


Fig. 1. Schematics and imaging functionalities of ML with $n = 1$ (conventional ML) and SIML with $n = 3$ respectively. Related results of conventional ML are shown in the left column of the figure and the right column presents related results of SIML. (a) Schematic diagram of a semi-infinite conventional ML with a gradient RI profile along x-axis direction and light trajectories from a point source in the lens. (b) Schematic diagram of a semi-finite SIML with a gradient RI profile along x-axis direction and light ray trajectories from a point source in the lens. Multiple focusing points are formed along y-axis direction at the edge. (c)–(d) Calculated electric field intensity distributions and the corresponding FWHM of the semi-infinite conventional ML and SIML. The red curves present the normalized electric field intensity along y-axis direction distance 1 from the bottom edge of the lens and the related FWHM is marked. (e)–(f) In the two semi-infinite MLs, a pair of identical point sources with a spacing of $(1/3)\lambda$ was severed as excitation sources at the wavelength of 10 and the electric field intensity distributions are shown respectively. (g)–(j) The truncated conventional ML and SIML with finite size and the related imaging performance. The black solid lines denote the boundary of the lens.

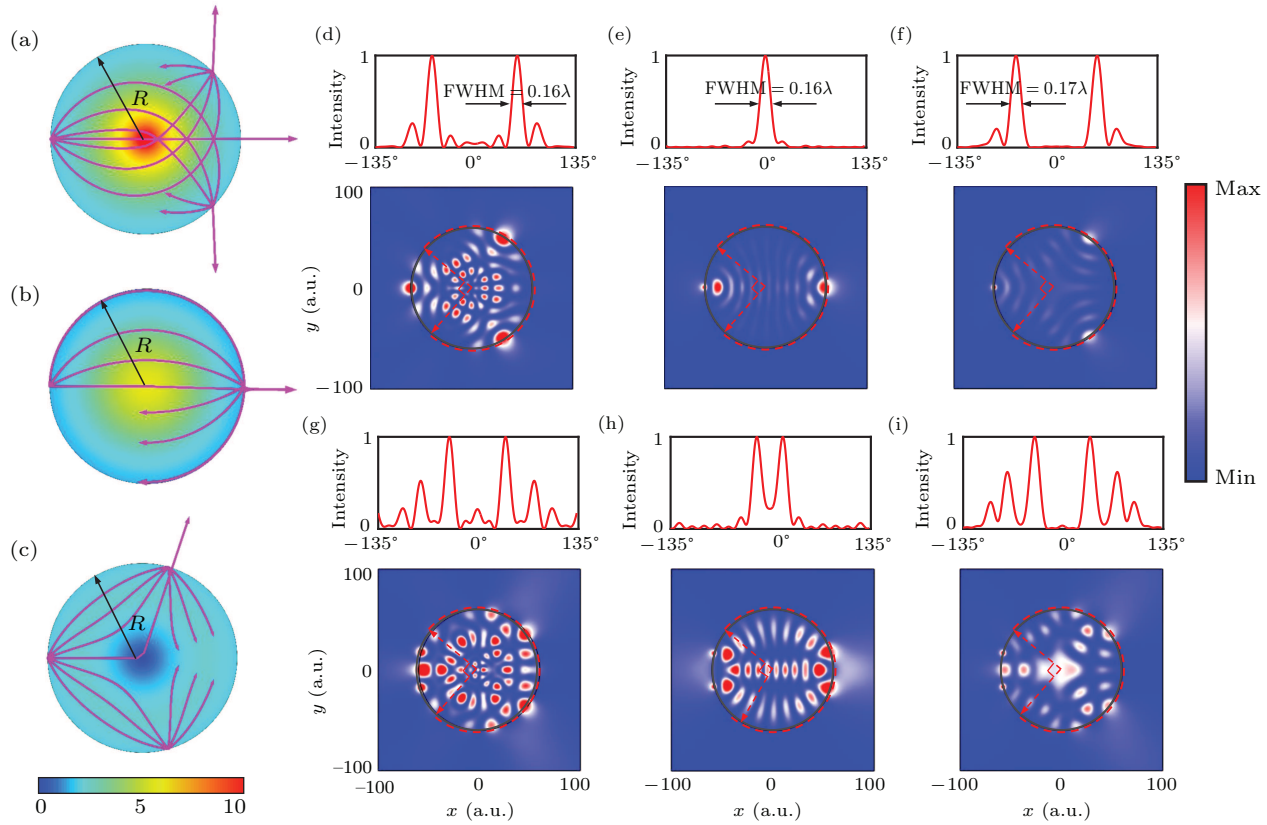


Fig. 2. Schematics and super-resolution imaging functionalities of the modified SIGMFELs with $\beta = 0.8$, 1, and 1.7, respectively. (a)–(c) Schematic diagram of the modified SIGMFELs with a gradient RI profile and light trajectories in the lenses for $\beta = 0.8$, 1, and 1.7, respectively. All the rays emitting from the point source are converging at the edge of the lenses and a part of the light rays are reflected respectively. (d)–(f) The super-resolution imaging performance of the modified SIGMFLs with the value of $\beta = 0.8$, 1, and 1.7 with a point source at the wavelength of 10 respectively. The corresponding FWHM at three different SIMFELs are marked. (g)–(i) Imaging performance of the three modified SIGMFELs of which two points sources with a spacing of $(1/3)\lambda$ are placed at the edge of the lens at the wavelength of 10. The red curves present the normalized electric field intensity along a concentric arc with a radius 61 of the lens from $-135°$ to $135°$ at the air imaging plane and the related FWHMs are marked respectively.

For the above problem, we propose the modified SIGMFEL without extreme RI profile and it can keep functionality of super-resolution imaging as same the original SIGMFEL. To design the modified SIGMFEL, we start with a optimized truncated SIML ($(0 \le x \le 4,\ 0 \le y \le 5L/2)$) with the RI profile $n = n_0 \operatorname{sech}(\beta x)$ where $n_0 = 3$ which can realize super-resolution imaging. Utilizing the same exponential conformal transformation mapping $w = \exp(-z(x,y))$, based on the truncated SLML with $\beta = 0.8$, 1, and 1.7, we obtain three annular SIGMFELs with outer radius $R_o = 60$ and inner radius $R_i = \exp(-4)R_o$ as shown in Figs. 3(a)–3(c). The relative RI distribution satisfies

$$n = \begin{cases} \dfrac{2n_0}{(r/R_o)^{1+\beta} + (r/R_o)^{1-\beta}}, & R_i \le r \le R_o, \\ 1, & r \le R_i, \end{cases} \tag{3}$$

where r is the distance from the center of the lens and R_o denotes the outer radius and $n_0 = 3$ is ambient RI. Therefore, the extreme RI at the central region is removed from the lens. According to transformation optics, we can deduce that the three modified SIGMFELs will maintain the property of super-resolution imaging which is consistent with that of the truncated SIML.

To further verify the super-imaging of the lens, a pair of point sources with a spacing of $(1/3)\lambda$ are located at the edge of the lens as an excitation source at same wavelength. In Figs. 2(g)–2(i), the electric filed intensity is clearly shown. The related normalized electric field intensity of the air imaging plane, along a concentric arc with a radius 61 of the lens from $-135°$ to $135°$, are shown by the red solid curve. The four obvious peaks in the figures represent the imaging points. It is clear that the modified SIGMEL with $\beta = 0.8$ and 1.7 can resolve the two sources with spacing of $(1/3)\lambda$ and achieve multiple super-resolution imaging. For SIGMFEL with $\beta = 0.8$ and 1.7, they can resolve the two source points and achieve multiply super-resolution imaging. For SIGMFEL with $\beta = 1$, it only achieves single super-resolution imaging.

Therefore, we prove that the three modified SIGMFEL can overcome the diffraction limit and realize super-resolution imaging. However, for the value of β is not equal to 1, the RI profile of SIGMFEL at center tends to the extreme value, which is a big barrier to fabrication and application. For β less than 1, the RI profile of the lens gradually increases to infinity from the edge to the center. For β more than 1, the RI profile of the lens gradually decreases to 0 from the edge to the center. If the extreme RI profile of the lens can be adjusted within feasible range and at the same time the modified lens maintains its original functionality, the applications for super-resolution imaging will be highly anticipated.

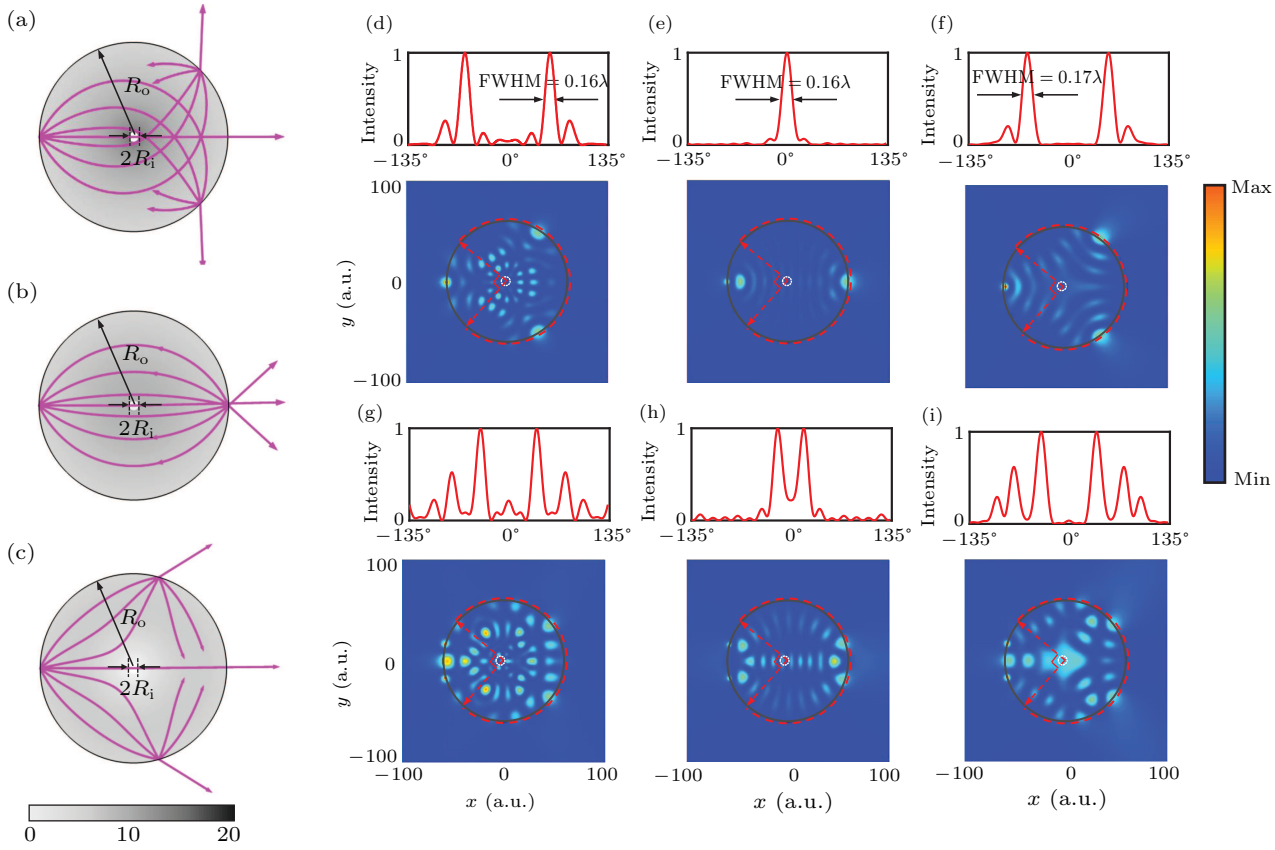


Fig. 3. Schematics and super-resolution imaging functionalities of the modified SIGMFELs with $\beta = 0.8$, 1, and 1.7, respectively. (a)–(c) Schematics of the modified SIGMFELs with a gradient RI profile and light trajectories in the lenses for $\beta = 0.8$, 1, and 1.7, respectively. All the rays emitting from the point source are converging at the edge of the lenses and a part of the light rays are reflected respectively. (d)–(f) Analysis of super-resolution imaging performance of the modified SIGMFLs with the value of $\beta = 0.8$, 1, and 1.7 with a point source at the wavelength of 10 respectively. The corresponding FWHM at three different SIMFELs are marked. It is far below the diffraction limit. (g)–(i) Imaging performance of the three modified SIGMFELs of which two points sources with a spacing of $(1/3)\lambda$ are placed at the edge of the lens. The red curves present the normalized electric field intensity along a concentric arc with a radius 61 of the lens from $-135°$ to $135°$ at the air imaging plane and the related FWHMs are marked respectively.

To verify the performance of super-resolution imaging for the modified SIGMFEL with three values of $\beta = 0.8$, 1, and 1.7, raytracing simulation and full-wave numerical simulation are performed at the wavelength of 10, respectively. A point source is located at $x = -60$ and $y = 0$ to excite a cylindrical TE wave. Figures 3(a)–3(c) display the imaging performance and reflection at the lens/air interface for three value of $\beta = 0.8$, 1, and 1.7 respectively. The figures also illustrate the RI distribution of modified SIGMFEL with three values of $\beta = 0.8$, 1, and 1.7, respectively. Perfect geometric focusing and reflection happen at the lens/air interface. Figures 3(d)–3(f) show electric field intensity distribution in the three lenses and the related FWHMs are marked. It is clear that the corresponding FWHM is less than 0.2λ, which is far below the diffraction limit. The imaging performance of the modified SIGMFEL agrees well with the original GMFEL. This demonstrates that the modified SIGFEL can achieve super-resolution imaging as well. To further verify the super-imaging performance of the three modified SIGMFELs, full-wave numerical simulation is performance with a pair of identical point sources of spacing of $(1/3)\lambda$ at the wavelength of 10. The related electric field intensity distribution and normalized electric field intensity at the air imaging plane are shown in Figs. 3(g)–3(i). Four tiny spots emerge at the edge of the two lenses with $\beta = 0.8$ and 1.7 respectively in Figs. 3(g) and 3(i). The red solid curves present the normalized electric field intensity at the air imaging plane, where the four obvious peaks in the figures represent the imaging points. It is clear that the modified SIGMEL with $\beta = 0.8$ and 1.7 can resolve the two sources with spacing of $(1/3)\lambda$ and achieve multiple super-resolution imaging. The modified SIGMEFL with $\beta = 1$ resolves the two sources with deep subwavelength spacing and the related normalized electric field intensity is shown by the red solid curve in Fig. 3(b). Therefore, we prove that the three modified SIGMFEL can overcome the diffraction limit and realize super-resolution imaging.

3. Conclusion

Enlightened by solid immersion lenses, we introduce the TIR mechanism to excite evanescent waves at the lens/air interfaces for multiple super-resolution imaging of the SIML. Utilizing conformal mapping, we derive the RI profile SIGMFEL from the SIML. The SIML and the SIGMFEL could be used to overcome the diffraction limit. However, the extreme

RI profile of the SIML and SIGMFEL have difficulties in fabrication and application. To circumvent the problem, we design a truncated SIML and a modified SIGMFEL without the extreme RI profile and verify the validity of the lenses for super-resolution imaging. The effect is robust and valid for broadband frequencies. It provides feasible designs for overcoming the diffraction limit from microwave to optical frequencies and may pave ways for multiple super-focusing, real-time bio-molecular imaging, nanolithography, high capacity information transmission waveguide. Especially, for the SIGMEL, the high-resolution multichannel waveguide coupler, multichannel waveguide crossing may be designed by transformation optics.

Acknowledgements

Project supported by the National Natural Science Foundation of China (Grant No. 92050102), the National Key Research and Development Program of China (Grant No. 2020YFA0710100), and the Fundamental Research Funds for Central Universities, China (Grant Nos. 20720200074, 20720220134, 202006310051, and 20720220033).

References

[1] Hecht B, Sick B, Wild U P, Deckert V, Zenobi R, Martin O J F and Pohl D W 2000 *J. Chem. Phys.* **112** 7761
[2] Pendry J B 2000 *Phys. Rev. Lett.* **85** 3966
[3] Veselago V 1968 *Sov. Phys. Usp.* **10** 509
[4] Shelby R A, Smith D R and Schultz S 2001 *Science* **292** 77
[5] Fang N, Lee H, Sun C and Zhang X 2005 *Science* **308** 534
[6] Taubner T, Korobkin D, Urzhumov Y, Shvets G and Hillenbrand R 2006 *Science* **313** 1595
[7] Smolyaninov I I, Hung Y J and Davis C C 2007 *Science* **315** 1699
[8] Liu Z W, Durant S, Lee H, Pikus Y, Fang N, Xiong Y, Sun C and Zhang X 2007 *Nano Lett.* **7** 403
[9] Zhang X and Liu Z W 2008 *Nat. Mater.* **7** 435
[10] Huang T J, Yin L Z, Zhao J, Du C H and Liu P K 2020 *ACS Photon.* **7** 2173
[11] Bi Y G, Peng L, Yang B, Ma S J, Chan H C, Xiang Y J and Zhang S 2021 *Optica* **8** 249
[12] Jacob Z, Alekseyev L V and Narimanov E 2006 *Opt. Express* **14** 8247
[13] Liu Z W, Lee H, Xiong Y, Sun C and Zhang X 2007 *Science* **315** 1686
[14] Rho J, Ye Z L, Xiong Y B, Yin X, Liu Z W, Choi H, Bartal G and Zhang X 2010 *Nat. Commun.* **1** 1
[15] Lu D and Liu Z W 2012 *Nat. Commun.* **3** 1
[16] Yuan G H, Rogers E T and Zheludev N I 2017 *Light Sci. Appl.* **6** e17036
[17] Rogers E T, Lindberg J, Roy T, Savo S, Chad J E, Dennis M R and Zheludev N I 2012 *Nat. Mater.* **11** 432
[18] Shen Y X, Peng Y G, Cai F Y, Huang K, Zhao D G, Qiu C W, Zheng H R and Zhu X F 2019 *Nat. Commun.* **10** 1
[19] Berry M V and Popescu S 2006 *J. Phys. A: Math. Gen.* **39** 6965
[20] Huang F M, Zheludev N, Chen Y and Javier Garcia de Abajo F 2007 *Appl. Phys. Lett.* **90** 091119
[21] Mansfield S M and Kino G S 1990 *Appl. Phys. Lett.* **57** 2615
[22] Fletcher D A, Crozier K B, Guarini K W, Minne S C, Kino G S, Quate C F and Goodson K E 2001 *J. Microelectromech. Syst.* **10** 450
[23] Mason D R, Jouravlev M V and Kim K S 2010 *Opt. Lett.* **35** 2007
[24] Kim M S, Scharf T, Haq M T, Nakagawa W and Herzig H P 2011 *Opt. Lett.* **36** 3930
[25] Bogucki A, Zinkiewicz L, Grzeszczyk M, Pacuski W, Nogajewski K, Kazimierczuk T, Rodek A, Suffczynski J, Watanabe K, Taniguchi T, Wasylczyk P, Potemski M and Kossacki P 2020 *Light Sci. Appl.* **9** 48
[26] Zhu H, Fan W, Zhou S X, Chen M and Wu L M 2016 *ACS Nano* **10** 9755
[27] Novitsky A, Repän T, Malureanu R, Takayama O, Shkondin E and Lavrinenko A V 2019 *Phys. Rev. A* **99** 023835
[28] Fan W, Yan B, Wang Z B and Wu L M 2016 *Sci. Adv.* **2** e1600901
[29] Wu Q, Turpin J P and Werner D H 2012 *Light Sci. Appl.* **1** e38
[30] He C, Chang J T, Hu Q, Wang J Y, Antonello J, He H H, Liu S X, Lin J Y, Dai B, Elson D S, Xi P, Ma H and Booth M J 2019 *Nat. Commun.* **10** 12286
[31] Li S Y, Zhou Y Y, Dong J J, Zhang X L, Cassan E, Hou J, Yang C Y, Chen S P, Gao D S and Chen H Y 2018 *Optica* **5** 1549
[32] Forbes A 2019 *Light Sci. Appl.* **8** 1
[33] Scopelliti M G and Chamanzar M 2019 *Light Sci. Appl.* **8** 65
[34] Ma H F and Cui T J 2010 *Nat. Commun.* **1** 1126
[35] Kundtz N and Smith D R 2010 *Nat. Mater.* **9** 129
[36] Zhang Y, He Y, Wang H W, Sun L and Su Y K 2020 *ACS Photon.* **10** 0c01269
[37] Leonhardt U 2009 *New J. Phys.* **11** 093040
[38] Leonhardt U and Philbin T G 2010 *Phys. Rev. A* **81** 011804
[39] Tao S C, Zhou Y Y and Chen H Y 2019 *Phys. Rev. A* **99** 013837
[40] Zhou Y Y, Hao Z L, Zhao P F and Chen H Y 2021 *Phys. Rev. Appl.* **17** 034039
[41] Tyc T, Herzánová L, Šarbort M and Bering K 2011 *New J. Phys.* **13** 115004
[42] Mikaelian A L and Prokhorov A M 1980 *V self-focusing media with variable index of refraction* (Amsterdam: Elsevier) pp. 279–345
[43] Wang X Y, Chen H Y, Liu H, Xu L, Sheng C and Zhu S N 2017 *Phys. Rev. Lett.* **119** 033902
[44] Peng H Y, Liu S L, Wu Y Z, Yan Y, Zhou Z C, Li X C, Bao Q L, Xu L and Chen H Y 2020 *Phys. Rev. Appl.* **13** 034050
[45] Kotlyar V V, Kovalev A A and Soifer V A 2011 *Optical Memory and Neural Networks (Information Optics)* **19** 273
[46] Sun F, Ma Y G, Ge X V and He S L 2013 *Opt. Express* **21** 7328
[47] Xu L and Chen H Y 2014 *Nat. Photon.* **9** 15
[48] Leonhardt U 2006 *Science* **312** 1777
[49] Yin Y H, Li J and Chen H Y 2020 *Opt. Express* **28** 37218
[50] Luneburg R K 1964 *Mathematical theory of optics* (California: University of California Press)
[51] Chen H Y 2018 *Phys. Rev. A* **98** 043843